Applied Chemical Engineering (2025) Volume 8 Issue 2 ISSN: 2578-2010 (O)
doi: 10.59429/ace.v8i2.5681

RESEARCH ARTICLE

Batch adsorption of methyl orange dye from solutions using nano-magnetic Fe/Mn-modified activated carbon derived from lignocellulosic biomass: Kinetics and thermodynamics

Asraa Awad Ali Hashim, Nahla Shakir Salman*

Department of Chemistry, College of Education, University of Al-Qadisiyah, Diwaniyah, 54004,Iraq

***Corresponding author:** Nahla Shakir Salman, nahla.shaker@qu.edu.iq

ABSTRACT

Recently, water pollution with dyes is one of the most serious problems and the most dangerous to human health and living organisms. This study involves the synthesis of magnetic nano form of Fe-Mn binary oxide modified biomass derived of agricultural waste commercial (wood shavings) as a raw material. Magnetic nanoparticles were prepared from activated carbon obtained from lignocellulose through chemical activation of wood shavings using NaOH incorporated with (FeCl3.6H2O), ferrous sulphate heptahydrate (FeSO4.7H2O) and potassium permanganate (KMnO4) for effective removal of MO dye from aqueous solutions in a batch processes. This material was characterized through several advanced techniques such as Fourier transform infrared Spectroscopy (FTIR), X-ray diffraction (XRD), Field Emission Scanning Electron Microscopy (FE-SEM), Thermo gravimetric analysis (TGA), Energy -dispersive X-ray spectroscopy (EDS), Transmission electron Microscopy (TEM) and Vibration sample magnetometer (VSM). These analysis techniques highlighted the successful synthesis of magnetic nanocomposite with a porous structure. Batch adsorption experiments were studied by including contact time, adsorbent dose, pH, and temperature to determine the optimal conditions for maximum dye removal efficiency. The developed LB-Fe/Mn nanocomposite demonstrated excellent removal efficiency (98.16%) for methyl orange, outperforming many current advanced materials. Thermodynamic study revealed the endothermic and spontaneous nature of studied process. Adsorption kinetics followed a pseudo-second-order model ($R^2 = 0.9676$), while Freundlich ($R^2 = 0.9544$) and Temkin ($R^2 = 0.9545$) isotherms best described the equilibrium data, indicating multilayer adsorption on heterogeneous surfaces with abundant binding sites.

Keywords: Adsorption; activated carbon; agricultural waste; batch adsorption; Fe/Mn nanocomposite; lignocellulosic biomass; methyl orange; wastewater treatment

ARTICLE INFO

Received: 15 June 2025
Accepted: 4 July 2025
Available online: 18 July 2025

Abbreviations

AC — Activated Carbon

BET — Brunauer–Emmett–Teller

BJH — Barrett–Joyner–Halenda

EDS — Energy-Dispersive X-ray Spectroscopy

FE-SEM — Field Emission Scanning Electron Microscopy

FTIR — Fourier Transform Infrared Spectroscopy

LB — Lignocellulosic Biomass

MO — Methyl Orange

PSO — Pseudo-Second-Order

PFO — Pseudo-First-Order

TGA — Thermogravimetric Analysis

TEM — Transmission Electron Microscopy

VSM — Vibrating Sample Magnetometry

XRD — X-ray Diffraction

1. Introduction

Water is the basis of life for all living organisms. With out water, life would cease to exist. In recent decades, cases of fresh water shortage have been observed, the accelerated growth in various parts such as industries including leathers, textile, food processing, paint, paper, plastics and pharmaceuticals is a major source of water pollution. Water pollution caused by industrial chemical releases is a major source of concern[1-10]. Dyes pose a significant threat to aquatic life and contribute to water pollution. Their presence alters the natural pigmentation and properties of water, making it harmful to aquatic organisms. Furthermore, a large amount of hazardous chemicals used in dyes can be carcinogenic[11, 12]. Consequently, removing dyes from textile wastewater has become a major environmental challenge[13-16] Azo dyes are widely used and are the largest and most important category of colors .The most characteristic feature of these dyes is having one or more azo groups (-N=N-) that act as a bridge between two stable organic parts of the dye and at a minimum one of these groups is aromatic that make them difficult to decompose[17-19]. The release of these substances in the environment is the biggest source of pollution for ecosystems[20-22]. In addition, these substances are also converted to aromatic amines through various processes as hydrolysis, oxidation, and other reactions, that are carcinogens[23-25].

Methyl orange is a common anionic azo dye that is harmful to biology and the environment, therefore, it must be removed from water[26-29]. The main processes to remove pollutants from water include, biodegradation[30], sedimentation chemistry, coagulation, advanced oxidation[31], ion exchange, adsorption[32, 33], filtration, and others but most of them find limited uses due to their high prices[34-38]. However, adsorption is an efficient process, user-friendly, cost effective and simple method[19, 39] which is widely used for removal of dyes from water[40]. Various adsorbents were used for the adsorption that include industrial or agricultural waste products as rice husk, a straw, coir, sawdust and corn cobs, lignocellulose materials[41-48], activated carbon, walnut shells[49], kaolin[50] and others[51-53]. Activated carbon is the most widely used adsorbent in industry due to its high surface area, porous structure and adsorptive efficiency. It can be derived from biomass resources by different chemically activating agent as HCl, H_3PO_4, H_2SO_4, $ZnCl_2$, Na_2CO_3, KOH, K_2CO_3 and NaOH[44]. Biomass is a residue from plant or animal that can be converted into biochar, high value products by different thermochemical techniques as pyrolysis, combustion, gasification and liquefication[54, 55]. Lignocellulosic biomass (LB), readily available in materials like straw and wood, is a rich source of cellulose, hemicellulose, lignin, and various other organic compounds. This has led to increased interest in using lignocellulose-derived materials as adsorbents. Cellulose and hemicellulose are composed of hexose and pentose sugar monomers, respectively, while lignin consists of polyphenolic aromatic compounds. In recent decades, scientists have focused on modifying lignin and its composition to create improved lignin-derived adsorbents. These modified materials possess excellent properties, making them valuable for removing dyes and organic matter from wastewater[56, 57]. Biochar can be used as an adsorbent for removal of various contaminants from wastewater, due to low-cost, high-energy efficiency and environment friendly nature[58-60].

In this study, a magnetic nanocomposite adsorbent was synthesized and modified by incorporating iron salts. Fe-Mn/AC magnetic nanoparticles were prepared using activated carbon derived from lignocellulose. The lignocellulose underwent hydrolysis, followed by physical and chemical activation. Subsequently, ferric, ferrous, and permanganate were added through a nanotechnology-based coprecipitation method to create the magnetic properties. The addition of ferric chloride was effective in increasing the magnetic properties and

enhancing the porosity of biomass[61]. Dried lignocellulose was chemically activated by impregnating it with NaOH. This method, as referenced in previous studies[62] is preferred due to NaOH's effectiveness as an activating agent, its low corrosivity, and its cost-effectiveness[63].

While numerous studies have explored biomass-derived adsorbents, many demonstrate only moderate removal efficiencies, limited reusability, or an absence of magnetic separability. There is a notable gap in the literature regarding a comprehensive examination of how Fe/Mn doping synergistically impacts lignocellulosic-based activated carbon for methyl orange (MO) removal, particularly when coupled with detailed investigations into its kinetics, thermodynamics, and reusability within batch adsorption systems. The innovative aspect of this research stems from successfully integrating magnetic separability, mesoporosity, and eco-friendliness into a single nanocomposite developed from lignocellulose. This study significantly contributes to existing knowledge by demonstrating superior removal efficiency and enhanced adsorption behavior compared to similar advanced adsorbents, all while upholding principles of sustainability and reusability. Findings underscore the promise of nanocomposites derived from agricultural waste as highly selective and effective materials for practical dye removal.

2. Experimental

2.1. Chemicals and materials

Waste wood shavings (**Figure 1a**), serving as the lignocellulose precursor, were collected from a local market. Sodium hydroxide (NaOH), potassium permanganate ($KMnO_4$), ferrous sulfate heptahydrate ($FeSO_4.7H_2O$), ferric chloride hexahydrate ($FeCl_3$.6H2O), and methyl orange (MO) (**Figure 1b**) were purchased from Scharlau, along with hydrochloric acid (HCl, 37 %). All materials used were of high purity and quality of nearly above 90%.

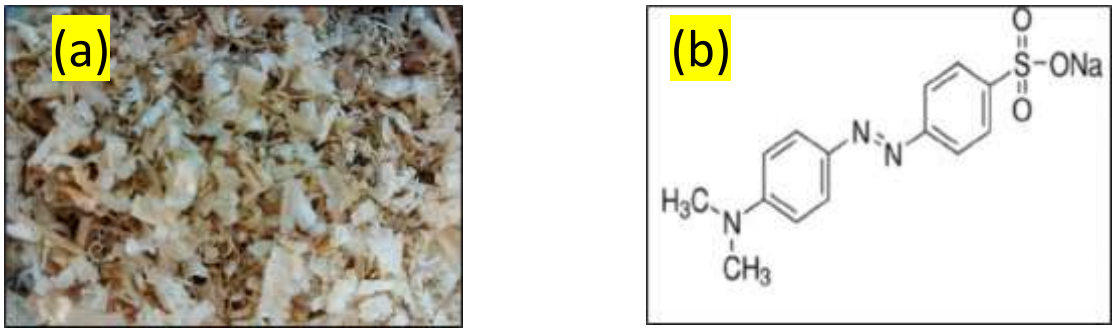

Figure 1. Image of (a) wood shavings and (b) chemical structural of MO dye

2.2. Preparation of adsorbent

Lignocellulosic raw material (wood shavings) was collected from a local market. The shavings were thoroughly washed with tap water, followed by deionized water, to remove impurities and achieve a constant pH. The cleaned material was then oven-dried at 105 °C for 4 hours until completely dry. The dried product was ground and sieved to a particle size of less than 0.25 mm[64]. Subsequently, 3g of the prepared lignocellulosic sample was impregnated with 50 ml of 10 % (wt) sodium hydroxide (NaOH) solution. This mixture was stirred magnetically at 400 rpm for 30 minutes at room temperature in a flask. A binary iron salt solution was prepared by dissolving 5 g of hydrated ferric chloride and 3 g of hydrated ferrous sulfate in 100 ml of deionized water. This solution was heated to 40 °C and stirred at 400 rpm in a flask on a heater with a magnetic stirrer for 30 minutes[65]. Next, a 1.5 % aqueous potassium permanganate ($KMnO_4$) solution was slowly added to the mixture of the 50 ml of 10 % NaOH solution and the lignocellulosic sample. This combined mixture was then slowly added to the binary iron salt solution while stirring for 3 hours at room temperature. Finally, the resulting Lignocellulose-Fe/Mn mixture was filtered, washed with deionized water until a pH of 7 was reached, and dried at 50 °C[66].

2.3. Characterization

The prepared adsorbent was characterized for its surface morphologies, crystalline structures, phase purity, functional groups, specific surface area, micropore volume, pore size distribution, elemental composition, chemical analysis, thermal properties, and magnetic properties. Surface morphologies were analyzed using field emission-scanning electron microscopy (SEM, Zeiss Libra 200 FE, Germany). Crystalline structures and phase purity were studied by X-ray diffractometry (XRD-6000, Shimadzu-Japan), using monochromatic nickel-filtered CuK (λ=1.5405 Å) radiation. Transmission electron microscopy (TEM) images, recorded with a Philips model FEL Quanta 400, were used to examine the morphology of the samples. Fourier transform infrared spectroscopy (FTIR) using a Shimadzu 8400s spectrophotometer was employed for characterization of different functional groups. The Brunauer-Emmett-Teller (BET) method was used to calculate the specific surface area (S_{BET}), micropore volume (V_m), and micropore and mesopore size distribution. Adsorption isotherms at variable relative pressures (P/P0) were also analyzed. Furthermore, pore size distribution was determined using the Barrett-Joyner-Halenda (BJH) technique. Elemental composition and chemical analysis were identified using energy-dispersive X-ray spectroscopy (EDX). The thermal properties of the samples were determined by thermogravimetry (TGA) under an air atmosphere, and magnetic properties were determined using a vibrating sample magnetometer (VSM, Meghnatis Daghigh Caviar Co).

2.4. Batch adsorption experiments

The adsorption efficiency of adsorbent for Methyl Orange was studied using batch experiments. Key parameters investigated included contact time (0-60 min), pH (2-10), adsorbent dose (0.01-0.1 g in 25 mL), initial dye concentration (60 ppm), and temperature (293-308 K). Adsorption experiments were conducted in 50 mL conical flasks, each containing 25 mL of 60 ppm dye solution. These flasks were placed in an orbital shaker and stirred at 120 rpm. After agitation, the suspension was centrifuged and then filtered. The filtrates were analyzed using a UV-visible spectrophotometer to measure absorbance at the maximum wavelength of the dye (λmax=464 nm). The removal efficiency (%R) and adsorption capacity (Q_e) were subsequently calculated using Equations (1) and (2), respectively [67, 68]:

$$Removal\ efficiency\ (\%)=(Ci-Ce)/Ci\ x100 \quad (1)$$

where: C_i (mg/L) refers to initial concentration and C_e refers to (mg/L) equilibrium concentration of dye at time t. The adsorption capacity Q_e (mg/g) represents the amount adsorbed at equilibrium and is calculated by the following equation [52, 69, 70]:

$$Qe=(Ci-Ce)V/m \quad (2)$$

where, V (L) is the of dye solution and m is weight (g) of adsorbent [71-73].

3. Results and discussion

3.1. Characterization of lignocellulose and magnetic adsorbent

FT-IR analysis of both lignocellulose and activated carbon (AC) was conducted in the elongation region 400 - 4000 cm^{-1} to identify functional groups and gains structural insights into the prepared materials[74, 75]. **Figure 2** illustrates the FT−IR spectra. A broadband spanning 3200−3600 cm^{-1} indicates overlapping O-H bonds, characteristic of hydroxyl, carboxylic, and phenolic group stretching vibrations within the lignocellulose and AC structures[76]. The absorption band at 2924.08 cm^{-1} corresponds to the symmetric and asymmetric stretching vibrations of CH_2 groups, prevalent in lignin and aliphatic compounds within both materials. A small, weak band at 1625.2 cm^{-1} suggests the presence of C=C bonds. The C-O bond in lignin and AC is identified by a single band at 1054 cm^{-1}. Peaks in the 500−650 cm^{-1} range are attributed to Fe-O and Fe-O-H stretching vibrations, confirming the formation of a magnetic adsorbent while preserving the lignocellulose's lignin structure[77, 78]. The strong absorption peak of Fe-O further indicates the successful

loading of lignocellulose onto Fe_3O_4. Additionally, sharpened Mn-O-H bending vibrations serve as evidence of significant lignin modification[79-83].

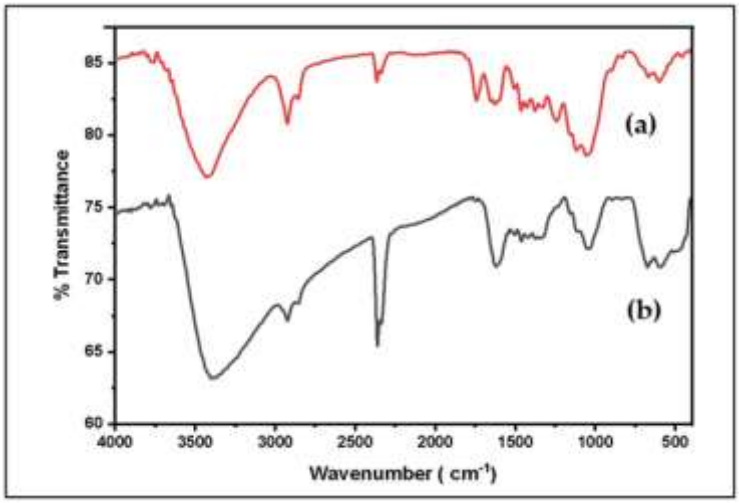

Figure 2. FTIR of lignocellulose and magnetic adsorbent

X-ray diffraction (XRD) patterns were utilized for primary characterization of pure lignocellulose and activated carbon magnetic (Fe_3O_4) nanoparticles, specifically to determine their crystallographic phases and changes in crystal structure [84]. The XRD patterns of these materials, presented in **Figure 3,** show strong peaks indicating good crystallinity and high purity. Peak broadening suggests the formation of activated carbon magnetic nanoparticles. A broad signal at 2θ = 20.52° and 22.3° was observed in the lignocellulose XRD spectrum [85], indicative of amorphous regions of lignin and hemicellulose. Additionally, the XRD spectrum of the composite lignin exhibits crystalline peaks at 2θ = 22.5°, 35.80° and 42.90° [86, 87]. Upon loading lignocellulose onto Fe_3O_4, the bands of the lignin nanocomposite appear broader, which implies a relatively small crystalline size for the nanoparticles. This not only affects the iron distribution within the particles but also influences their magnetic strength [80, 88, 89].

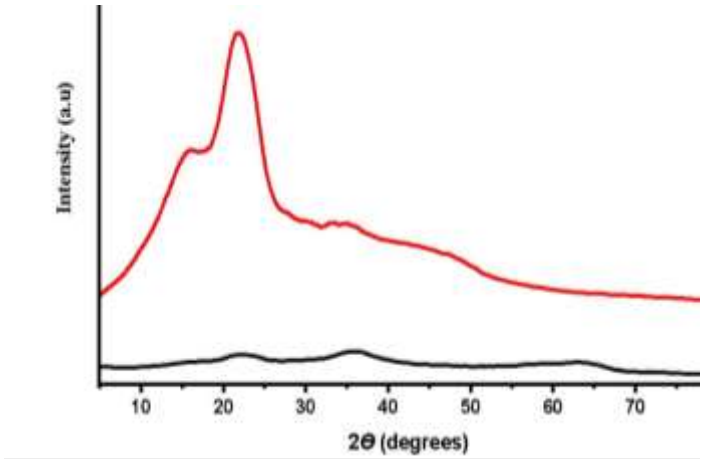

Figure 3. X-ray diffraction of (red line) raw lignocellulose and (black line) magnetic adsorbent

The surface morphology of the materials, including raw lignocellulose and Fe/Mn-loaded activated carbon (AC), was examined using Scanning Electron Microscopy (SEM) [90]. As shown in **Figure 4a,** raw lignocellulose exhibits a uniform, smooth, and porous surface. In contrast, the surface of the activated lignocellulose nanocomposite (**Figure 4b**) became rough, wrinkled, and homogeneous, which is beneficial for Methyl Orange (MO) dye adsorption. These findings indicate that the lignocellulose nanocomposite developed well-distributed, well-developed pores, leading to a porous system with a large surface area. After MO dye

adsorption, the pores and the surface of the lignocellulose nanocomposite were fully occupied by the dye. This further verifies the adsorption of MO dyes by the lignocellulose nanocomposite. The FESEM image in **Figure 4c,** taken after dye adsorption, revealed a smoother and more coherent surface. This suggests that the dye molecules completely covered the composite surface, thereby confirming adsorption [65, 91-94].

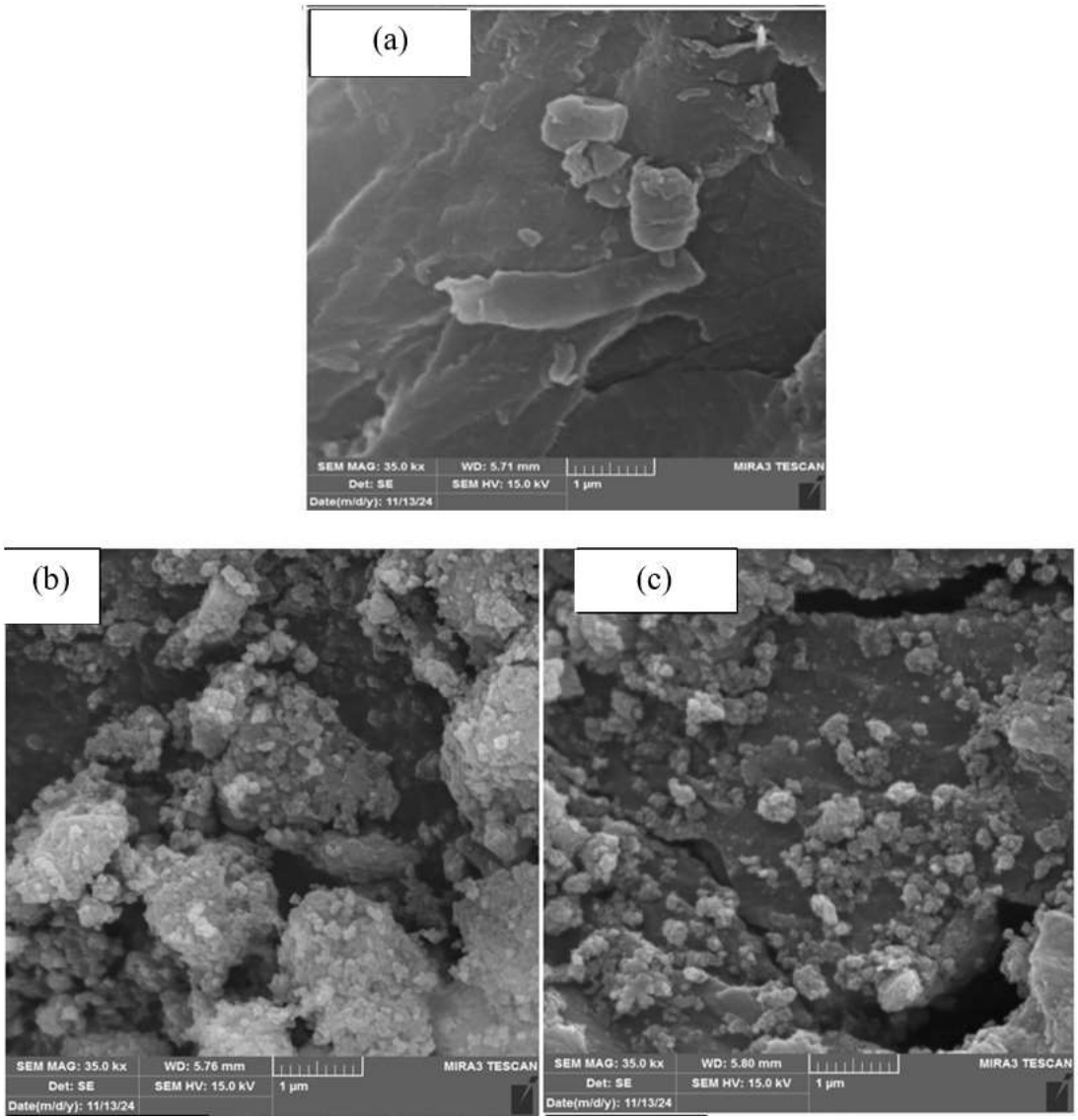

Figure 4. SEM of (a) raw lignocelloluse, (b) magnetic adsorbent and (c) magnetic adsorbent with MO

Energy-dispersive X-ray spectroscopy (EDS) elemental spectra and mapping (**Figure 5a, 3b**) for lignocellulose and the magnetic adsorbent, respectively, demonstrate the elemental composition of these materials. EDS analysis revealed that lignocellulose primarily consists of carbon (53.5%) and oxygen (45.3%), with smaller percentages of potassium (0.8%) and magnesium (0.3%). The results for the nanocomposite lignocellulose show a high percentage of iron (49%), followed by oxygen (22.2%), manganese (15.3%), and carbon (11.3%). These findings collectively indicate excellent modification of the lignocellulose [95-99]

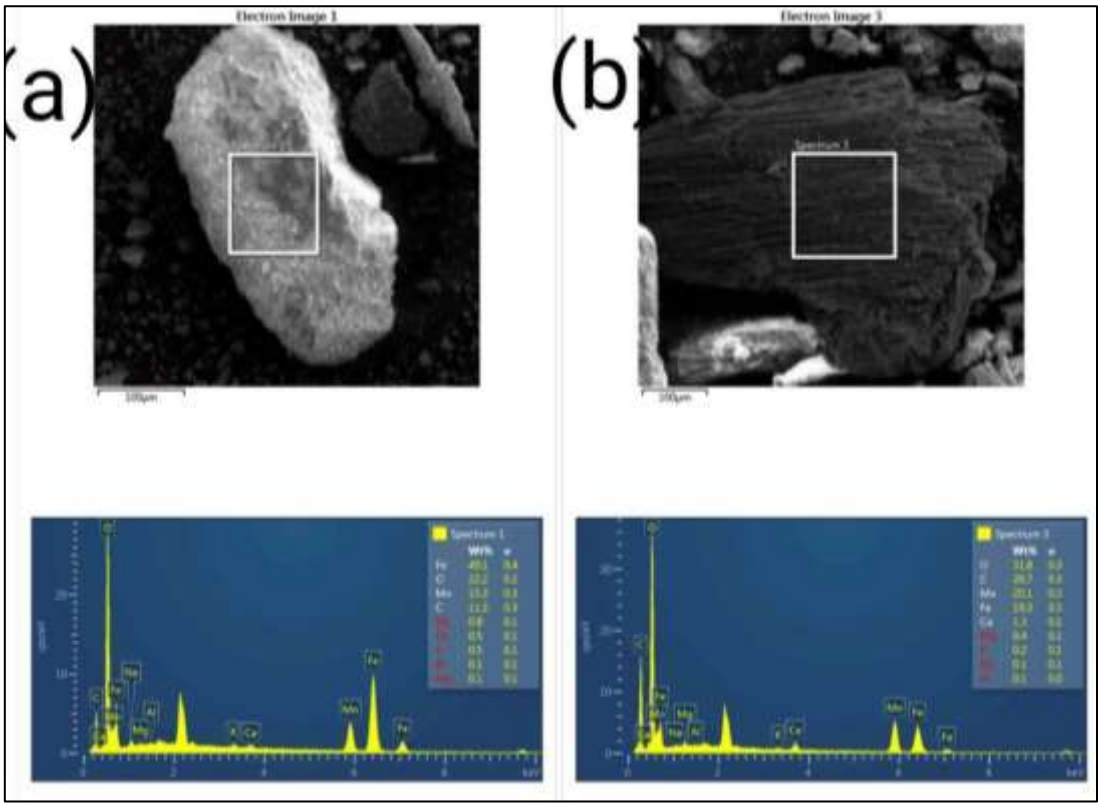

Figure 5. EDS of (a) lignocellulose and (b) magnetic adsorbent

Vibrating Sample Magnetometry (VSM) was employed to assess the magnetic properties of the nanocomposite-activated surface. This technique functions by measuring the magnetic response of the material through vibration. As depicted in the magnetization curves (**Figure 6a, 6b**), the saturated magnetization of the lignocellulose nanocomposite was determined to be approximately 12.5 emu g^{-1}. This value clearly demonstrates the improved magnetic properties of the activated surface in contrast to pure lignocellulose, which is non-magnetic. The observed superparamagnetic characteristic of new material broadens its use for large-scale adsorption applications, facilitating efficient separation of magnetic material via an external magnetic field[100-102].

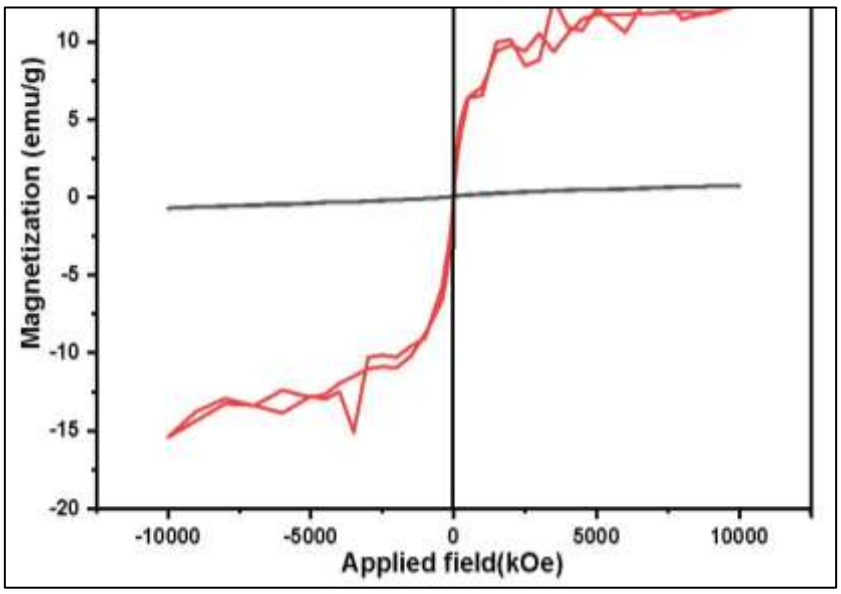

Figure 6. The magnetic properties of (red line) Lignocellulose and (black line) magnetic adsorbent

BET (Brunauer-Emmett-Teller) measurements are essential for determining specific surface areas of materials. This technique estimates a powder's specific surface area by analyzing the amount of nitrogen adsorbed onto its surface in relation to pressure, at the boiling temperature of liquid nitrogen under normal atmospheric pressure. The observations are then interpreted using BET theory, which explains physical adsorption of gas molecules onto solid surfaces. It's worth noting that particles of similar size can exhibit significant differences in surface area[103, 104]. **Figures 7a** and **7b** illustrate the N_2 adsorption-desorption isotherms and pore size distribution curves for both lignocellulose and lignocellulose-derived carbon material samples. **Table 1** presents the measured BET surface areas and pore volume data, with the BJH (Barrett-Joyner-Halenda) method used to analyze the pore size distribution curves. A notable observation is the substantial increase in BET surface area from 3.3119 m^2/g for lignocellulose to 161.3349 m^2/g for the nanocomposite lignocellulose. Concurrently, the pore volume increased from 0.004655 cm^3/g to 0.038557 cm^3/g. Generally, a greater surface area leads to enhanced adsorption due to an increased number of available adsorbing sites. Similarly, larger porosity also contributes to greater adsorption, explaining why finely divided and highly porous materials are excellent adsorbents. The mean pore diameter is also a critical factor influencing adsorption efficiency. The nanocomposite lignin material demonstrated superior characteristics, exhibiting a higher specific surface area (161.3349 m^2/g), increased porosity (0.038557 cm^3/g), and a higher BJH surface area (191.7337 m^2/g). These improvements are primarily attributed to its smaller particle size, as confirmed by XRD analysis. The observed decrease in BET surface area for lignocellulose compared to lignocellulose nanocomposite is likely due to the loading of lignin particles, which appear to cover most of mesopores and micropores. The pore size distribution curves, which appear broadly narrow, further indicate formation of mesoporous materials. According to the International Union of Pure and Applied Chemistry (IUPAC), solids are classified by pore size: microporous materials have pore sizes less than 2 nm, mesoporous materials have pore sizes between 2 nm and 50 nm, and macroporous materials have pore sizes greater than 50 nm [105, 106]. The pore size distribution of magnetic activated carbon from wood shavings suggests formation of a highly mesoporous structure [107]. Furthermore, based on IUPAC classification, these materials can be categorized as Type III with H3 hysteresis loops, indicating presence of slit-like mesopores formed between aggregated nanoparticles and an unrestricted multilayer formation process [108].

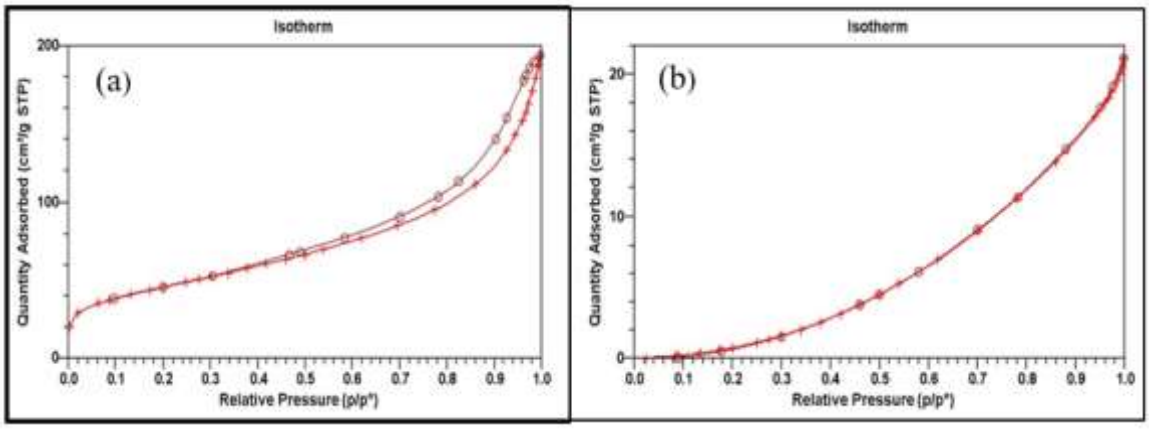

Figure 7. BET of (a) Lignocellulose and (b) magnetic adsorbent

Table 1. BET-BJH surface area and pore structure of Lignocellulose and magnetic adsorbent (LB-Fe/Mn)

Physicochemical properties	**LB**	**LB-Fe/Mn**
BET surface area, m^2/g	3.3119	161.3349
BJH surface area, m^2/g	24.769	191.7337
Pore Volume, cm^3/g	0.004655	0.038557
Pore Size, nm	11.8603	6.8954
Isotherm type	III	III
Hysteresis loop	H3	H3

Transmission Electron Microscopy (TEM) and High-Resolution TEM (HRTEM) were used to examine the morphology and particle size of lignocellulose and magnetic activated carbon, as shown in **Figure 8a-b.** This technique involves directing a beam of electrons at a sample. As these electrons pass through sample, an image is recorded, revealing its microstructure. Microstructural imaging of lignocellulose before modification provided baseline data (**Figure 8a**). In contrast, **Figure 8b**, depicting nanocomposite of activated lignocellulose, clearly shows formation of a mesoporous carbonaceous material. This material exhibits a range of pore sizes, from large to small, along with visible cracks on its surface. These features are a direct result of the lignocellulose's activation using potassium permanganate ($KMnO_4$), ferric chloride ($FeCl_3 \cdot 6H_2O$), and ferrous sulfate ($FeSO_4 \cdot 7H_2O$). The Fe_3O_4 nanoparticles, synthesized from Fe^{+3} and Fe^{+2} precursors, appear spherical and exhibit strong agglomeration. This agglomeration leads to a wide specific surface area, driven by various interactions as new quasi-chemical bonds, hydrogen bonds, static electricity, and intermolecular forces. However, when Fe_3O_4 nanoparticles are loaded onto lignocellulose, their agglomeration is suppressed, resulting in better dispersion. This increased stability is crucial as it facilitates adsorption process[80, 98, 109-111].

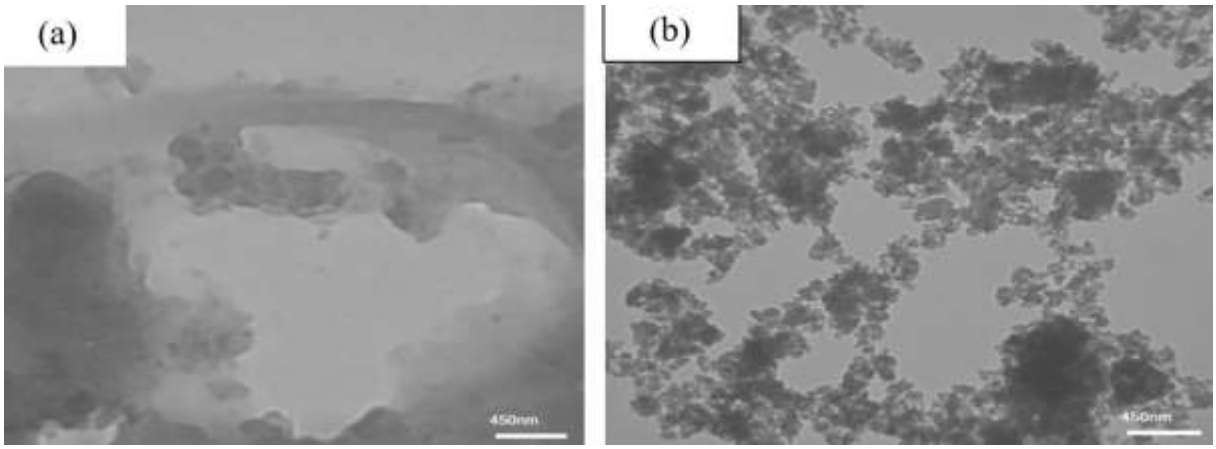

Figure 8. TEM results of (a) Lignocellulose and (b) magnetic adsorbent

Thermogravimetric Analysis (TGA) was employed to assess the thermal stability of synthesized materials. This analytical technique measures changes in a sample's weight as a function of time or temperature, performed using a TGA instrument under an inert nitrogen atmosphere [112]. **Figure 9** illustrates the thermal properties of the magnetic activated surface. The resulting thermogram, which plots mass loss against increasing temperature, provides crucial information about the material's thermal degradation. The thermogram of the magnetic activated lignocellulose nanocomposite was recorded within a temperature range of 40-800 °C under a nitrogen atmosphere (flow rate of 6 L/min). The analysis reveals three distinct weight loss steps (thermal dissociation) occurring in two main stages. The first stage of weight loss occurs between approximately 50-150 °C. This initial mass reduction is attributed to the loss of moisture, including absorbed water, water vapor, or residual organic solvents. It also accounts for the evaporation of various low molecular weight compounds from the fiber materials, as well as the dissociation of hydrogen bonds formed between the -OH groups in the nanocellulose structures and the fiber materials[113-115]. The second stage of significant weight loss for the magnetic activated surface begins roughly between 300-400°C. During this stage, a substantial decrease in weight is observed, primarily due to the loss of active functional groups, such as carboxyl groups (-COOH), and, most importantly, the depolymerization of cellulose and hemicellulose[116]. The third and final stage of weight loss commences within the range of 400-800°C, corresponding to the degradation of lignin within the nano-activated compound. Notably, only a slight weight loss continues at higher temperatures. This minimal mass loss at elevated temperatures indicates excellent thermal stability and high overall stability of surface, attributed to its activation with iron and manganese[117-119].

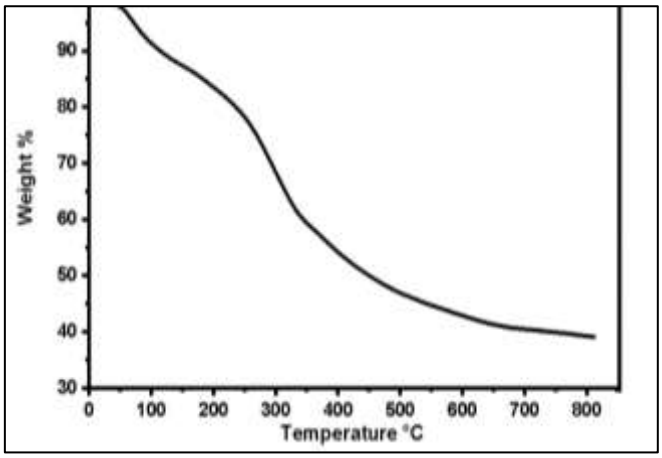

Figure 9. TGA curve of magnetic adsorbent

3.2. Effect of contact time

The equilibrium time is a critical factor influencing the efficiency and quantity of the adsorption process. In this study, the equilibrium time for the adsorption of Methyl Orange (MO) dye onto the activated magnetic surface was investigated. The adsorption of MO dye at a concentration of 60 ppm onto the adsorbent was evaluated under controlled conditions. Experiments were conducted at varying time intervals (0-60 minutes) in conical flasks, each containing 25 mL of MO dye solution. An adsorbent dose of 0.01 g was used, and the pH was maintained at 7, with a temperature of 25°C. A constant shaking velocity of 120 rpm was applied. After each agitation time, the samples were filtered and analyzed using a UV-Vis spectrophotometer (Shimadzu, Japan) at a maximum wavelength of 464 nm for MO dye. **Figure 10a** illustrates that the equilibrium state was gradually achieved at approximately 40 minutes. The initial removal percentage of MO dye was relatively rapid, which can be attributed to the high availability of active sites on adsorbent's surface. The removal efficiencies reached a steady value after the equilibrium time and then began to decrease. This subsequent reduction is likely due to slow diffusion of MO dye molecules into the adsorbent's pores once the external adsorption sites are fully occupied [120, 121].

3.3. Effect of adsorbent dose

The adsorbent dosage is a significant factor in the adsorption process, as it directly relates to the number of available active sites on the adsorbent's surface and helps determine the equilibrium between the adsorbent and the adsorbed dye (MO dye). In this study, the adsorption capacity and efficiency were investigated by varying the adsorbent (LB-Fe/Mn) dosage from 0.01 to 0.1 g/L. Experiments were conducted in 25 mL conical flasks containing an initial MO dye concentration of 60 ppm at a pH of 7. The solutions were agitated in a water bath shaker at a constant temperature of 25°C and a velocity of 120 rpm for 40 minutes, after which the absorbance of the solutions was measured. As shown in **Figure 10b**, the removal percentage increased from 51.83% to 75.17% as the adsorbent dosage was increased from 0.01 to 0.06 g/L. This increase in adsorption capacity and efficiency is attributed to the larger surface area and increased number of available active sites, facilitating more interactions between the adsorbent and MO dye molecules. Beyond 0.06 g/L, which is considered the optimal adsorbent dose, the adsorption process became restricted. This limitation occurs because all active sites on the adsorbent surface become occupied with dye molecules, leading to a state of saturation where the surface is almost entirely filled, and equilibrium is achieved. The subsequent decrease in removal percentage after saturation may be attributed to the overlapping and aggregation of adsorbent particles, which can hinder the diffusion of MO dye towards the adsorbent surface[122-125].

3.4. Effect of pH

The pH of the solution is one of the most crucial factors governing the sorption process, as it dictates the optimal medium (acidic or basic) for adsorption. This is due to its significant influence on the degree of ionization, the charge of the adsorbent surface, and the overall adsorption mechanism [126-130]. In this study, the effect of pH on the adsorption of Methyl Orange (MO) dye onto the activated magnetic surface was investigated across a range of 2-10. The pH of the initial MO dye solutions was adjusted using dilute NaOH and HCl (0.1 M). Experiments were conducted under ideal conditions, including a contact time of 40 minutes, an initial MO dye concentration of 60 ppm, an adsorbent dose of 0.06 g/L, and a temperature of 25 °C. As depicted in **Figure 10c,** the highest removal percentage of 93.129 % was achieved at pH 2 (strongly acidic). This indicates that a more acidic medium is favorable for the adsorption of MO dye. Given that MO dye is an anionic dye, it prefers an acidic environment for adsorption onto the activated surface. The enhanced adsorption in acidic media is attributed to the increased concentration of hydrogen ions and the resulting electrostatic attractive forces between the negatively charged MO dye molecules and the positively charged protons on the activated adsorbent surface. This protonation process leads to an increase in the positive charge density on the adsorbent. Conversely, the percentage adsorption of MO dye significantly decreases from 93.129 % to 40.068 % as the pH increases from 2 to 10. This reduction is due to a decrease in the attractive forces between the adsorbent and adsorbate, coupled with increasing repulsive forces [99, 131-135]. The point of zero charge (pH_{zpc}) is another vital factor to consider given the nature of the molecules involved. As shown in **Figure 10d,** the pH_{zpc} of the adsorbent surface was determined to be approximately 7.2. This means that when the solution pH is below 7.2, the adsorbent surface carries a net positive charge, facilitating attractive interactions with the anionic MO dye molecules and leading to increased adsorption. However, at pH values above 7.2, the adsorbent becomes negatively charged. In this scenario, adsorption of MO dye decreases due to electrostatic repulsion between the negatively charged adsorbent surface and the anionic dye molecules, as well as competition from OH^- ions.

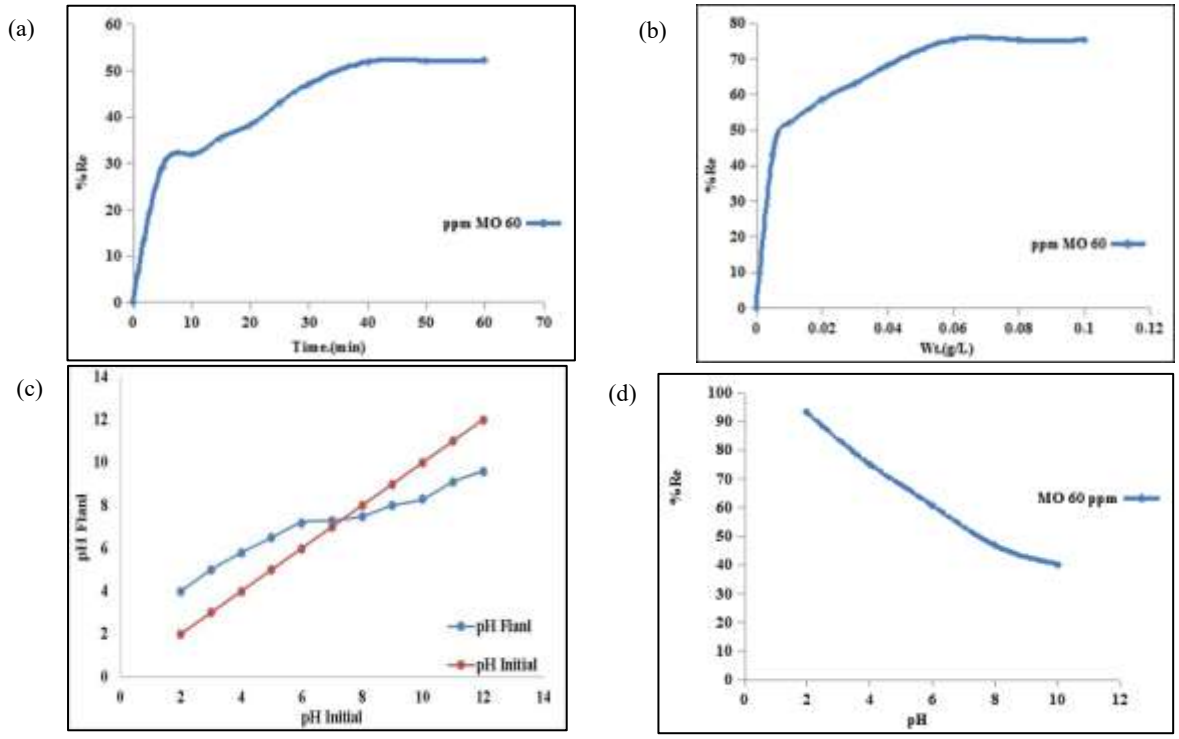

Figure 10. Effect of (a) contact time, (b) adsorbent dosage, (c) pH and (d) pH_{zpc} determination for adsorption process

3.5. Adsorption thermodynamics

Temperature is a critical factor that significantly influences the adsorption efficiency of MO dye onto an adsorbent. It also helps in determining whether the adsorption process is endothermic or exothermic and

reveals insights into the degrees of freedom of MO dye molecules during adsorption. To investigate the effect of temperature on MO dye uptake, experiments were conducted at temperatures ranging from 293 K to 308 K for 40 minutes, maintaining a fixed adsorbent weight of 0.06 g and a pH of 2. As shown in **Figure 11a,** an increase in temperature favored the transport of mobile adsorbate molecules into the pores of the activated surface, leading to an increase in the amount of MO dye adsorbed. This suggests that adsorption increases with rising temperature. Furthermore, increased temperature enhances the effective collisions between the adsorbent and MO dye molecules due to an increase in kinetic energy, facilitating more interactions between mobile molecules and active surface sites. This behavior clearly indicates that the adsorption process is endothermic, meaning it absorbs energy from its surroundings. This also implies that higher temperatures increase both the kinetic energy of the molecules and the speed of the adsorption process [136, 137]. This is evidenced by the increase in adsorption efficiency from 89.66% to 98.16% when temperatures increased within range of 298 K to 308 K. Understanding the thermodynamics of adsorption is crucial for characterizing the reaction's nature, including its spontaneity, bond strength, and system randomness. Thermodynamic functions can be determined by studying adsorption isotherms at various temperatures. Thermodynamics plays a pivotal role in the adsorption process through its fundamental laws. Parameters were calculated to explain the adsorption nature of this study, including Gibbs free energy change (ΔG), enthalpy change (ΔH), and entropy change (ΔS). The first and second laws of thermodynamics provide a framework for understanding energy transformations and entropy changes during adsorption, which are essential for optimizing adsorption systems. A negative ΔG indicates a spontaneous and favorable adsorption process. The heat of adsorption, reflected by ΔH, signifies the energy change during the process, influencing the adsorbent's capacity and selectivity. Changes in ΔS affect the thermodynamic feasibility and efficiency of adsorption. The adsorption process is often spontaneous and is accompanied by a decrease in the free energy of the surface. A positive value of entropy (ΔS) signifies an increase in the randomness of the solid/solution interface, likely because dye molecules become less restricted as they bind to the surface, forming bonds that increase their degrees of freedom. Moreover, the positive value of ΔH implies an endothermic adsorption process, indicating that the sorption process absorbs energy from its surroundings. The values for the entropy change, free energy change, and enthalpy change were calculated using the Van't Hoff equation (Equations 3, 4, and 5)[52, 138, 139]:

$$\Delta G = \Delta H - T\Delta S \tag{3}$$

The heat of adsorption quantifies the thermal energy released or absorbed when a specific amount of material adsorbs onto an adsorbent surface. This value is crucial for understanding the strength and type of bonds formed between the adsorbate molecules and the adsorbent surface. A comprehensive thermodynamic description of the adsorption process necessitates knowledge of the reaction's coefficients and conditions, particularly the enthalpy (ΔH) and entropy (ΔS) functions of the system. The Gibbs free energy change (ΔG) can be calculated directly from the equilibrium constant (K_e) at specific temperatures. This thermodynamic analysis provides vital insights into the spontaneity and driving forces behind the adsorption phenomenon [140-142].

$$\Delta G = -RT \ln Keq \tag{4}$$

where: ΔG = free energy change (kJ/mol), K_{eq}= equilibrium constant for adsorption process, R = ideal gas constant (8.314 J/K.mol) and T = absolute temperature measured in kelvin.

$$lnKeq = \frac{\Delta S}{R} - \frac{\Delta H}{RT} \tag{5}$$

The value of ΔG can be calculated from thermodynamic equilibrium constant (K_{eq}) at specific temperatures. The other thermodynamic parameters can be determined from slope and intercept of a plot of $\ln K_{eq}$ versus 1/T, as shown in **Figure 11b.** The calculated thermodynamic parameters are listed in **Table 2**

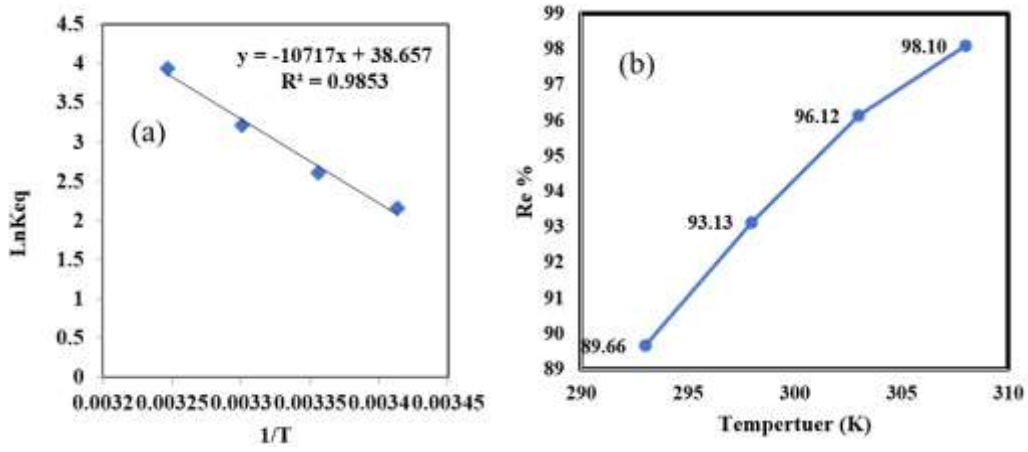

Figure 11. (a) Effect of temperature on MO dye adsorption and (b) Van't Hoff plot

Table 2. Thermodynamic parameters of MO dye on LB-Fe/Mn

Adsorbate	Temp (K)	-Δ*G* (kJ/mol)	Δ*H* (kJ/mol)	Δ*S* (J/mol.K)
MO	293	-5.26174	89.10114	322.0576
	298	-6.45832		320.6693
	303	-8.08750		320.7546
	308	-10.0933		322.0597

3.6. Adsorption isotherm

Adsorption isotherms are graphical representations used to study the efficiency of an adsorption process, such as the removal of Methyl Orange (MO) dye from aqueous solutions by an activated surface. An adsorption isotherm plots the amount of dye adsorbed onto the adsorbent's surface against the equilibrium concentration of the dye solution. Essentially, it illustrates how much of a substance is adsorbed onto a solid surface at a constant temperature, as a function of its equilibrium partial pressure (or concentration in solution). In this study, several common adsorption isotherm models, including Freundlich, Langmuir, and Temkin, were employed to analyze the adsorption data. The Langmuir model is a widely used adsorption isotherm that describes the interaction between an adsorbate and an adsorbent based on several key assumptions. It postulates that the adsorbent surface is energetically uniform, meaning all adsorption sites are identical and have equal affinity for the adsorbate. Furthermore, the model assumes a fixed number of available vacant adsorption sites on the solid surface, and that adsorption occurs as a monolayer, where adsorbate molecules form only a single layer without significant multilayer formation. This model is valuable for understanding the extent to which adsorbent surface layers become saturated with the adsorbate material, such as methyl orange dye. The Langmuir equation expressed as [30, 53, 143-145].

$$\frac{1}{q_e} = \frac{1}{q_{max}} + \frac{1}{q_o b C_e} \quad (6)$$

Langmuir constant and maximal capacity for adsorption are denoted via b

(L/mg) and q_{max} ($\frac{mg}{g}$) correspondingly [146, 147]. **Figure 12 a** and **Table 3** represent results. The result evident, R_L (0.1835) is favorable and refers to Langmuir isotherm, and correlation coefficient (R^2) as 0.8657. The Freundlich adsorption isotherm is an empirical relationship that describes the adsorption of a solute onto an adsorbent surface in equilibrium with its concentration in the liquid phase. This model is particularly applicable for non-ideal sorption systems, where the active sites on the adsorbent surface are heterogeneous, and multilayer adsorption can occur. The Freundlich isotherm can be expressed as [148-152]

$$\log q_e = \log K_f + \frac{1}{n} \log C_e \quad (7)$$

Constant and exponent for Freundlich model (mg/g) are denoted via k_f and 'n'correspondingly [56]. In the Freundlich isotherm, the value of 1/n provides insight into the adsorption behavior. A value close to 1 indicates a normal Freundlich isotherm, while a value greater than 1 suggests a cooperative adsorption process. The Freundlich constants, k_F and n, were determined from the intercept and slope as shown in **Figure 12b.** The results yielded a high correlation coefficient (R^2) of 0.9544 for the Freundlich isotherm. This R^2 value is higher than that obtained for the Langmuir isotherm, indicating that the Freundlich isotherm provides a better fit for adsorption of MO dye in this study. The Temkin adsorption isotherm is employed to evaluate the adsorption potential between an adsorbent and an adsorbate within solution. This isotherm uniquely accounts for ion interactions within aqueous solution (adsorbent-adsorbent interactions). It operates on the assumption that the heat of adsorption decreases linearly for all molecules as surface coverage increases. This linear decrease is due to interactions between the activated adsorbent surface and the adsorbate molecules already present on surface. Essentially, as active sites become occupied, energy of subsequent adsorption events diminishes due to these interactions [147, 153-156].

$$q_{eq} = B\ln A_T + B\ln C_{eq} \quad (8)$$

here, R and B denotes constant of universal gas (J/mol K) and adsorption heat (J/mol), A_T, b_T and T corresponds to constant of Temkin equilibrium binding (L/ g), Temkin (in J/ mol) as well as temperature (K) correspondingly [157]. Results

As shown in **Figure 12c,** the parameters for the Temkin isotherm were determined from its slope and intercept. When comparing the R^2 values for all tested isotherms, the Temkin isotherm demonstrated the best fit for MO dye adsorption with an R^2 of 0.9545. It was closely followed by the Freundlich isotherm, which yielded an R^2 of 0.9544. The Langmuir isotherm showed the least suitable fit with an R^2 of 0.8657. These results indicate that both the Freundlich and Temkin models best represent the experimental adsorption data. This suggests that the sorption process likely occurs in a multilayer fashion on a heterogeneous adsorbent surface, characteristic of physical adsorption.

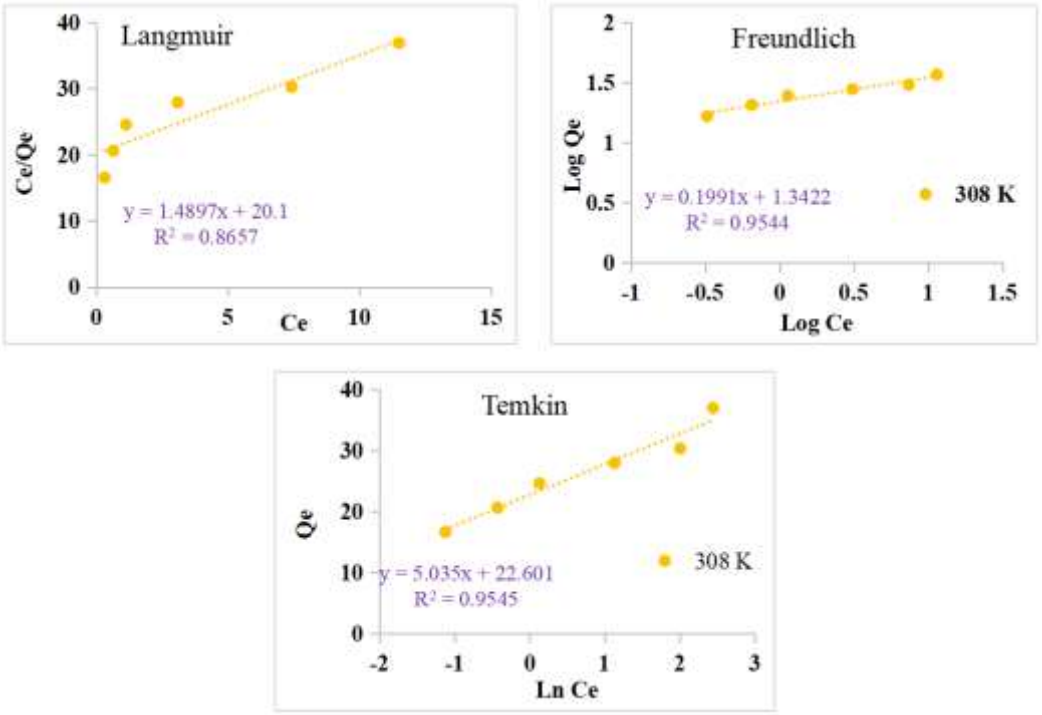

Figure 12. (a) Langmuir isotherm, (b) Freundlich isotherm and (c) Temkin isotherm for adsorption of MO dye

Table 3. Langmuir, Freundlich and Temkin isotherm for MO adsorption

Isotherm model	Isotherm parameters	MO
Langmuir	q_m (mg/g)	20.1
	b(L/mg)	0.07411
	R_L	0.1835
	R^2	0.8657
Freundlich	K_F (mg/g)	21.9887
	N	5.0226
	R^2	0.9544
Temkin	K_T (L/mg)	89.0126
	B	5.0350
	R^2	0.9545

3.7. Adsorption kinetics

The study of adsorption kinetics is crucial for effectively designing adsorption systems and optimizing process conditions over time. It provides insights into the reaction mechanism, reaction speed, and the rate-limiting step, in addition to revealing the nature of chemical interactions between the adsorbent surface and the dye. Furthermore, kinetic studies help identify the most appropriate kinetic model for a given adsorption process. To analyze the kinetics of Methyl Orange (MO) dye sorption, two commonly used models are employed: the pseudo-first-order (PFO) model and the pseudo-second-order (PSO) model. The pseudo-first-order model primarily describes adsorption driven by physical forces. It assumes that the rate of adsorption is proportional to the difference between the maximum adsorption capacity and the amount adsorbed over time, aligning with the concept of available sites on the adsorbent surface [98]. This model, based on the Lagergren equation, is often most suitable for lower solute concentrations [158] and considers both the initial and adsorbed amounts. This first-order rate equation, established to describe adsorption kinetics in liquid-solid systems, is represented by a specific relation. Its linear form is derived by plotting log(qe−qt) versus time. From the slope and intercept of this linear plot, the rate constant (k1) and equilibrium adsorption capacity can be determined, respectively (Equation 9) [159-164]:

$$Log\ (qe\text{-}qt) = Log\ qe - \left(\frac{k1}{2.303}\right)t \tag{9}$$

Pseudo second-order is based on the chemical reaction between the adsorbent and adsorbent, the equation is represented by Equation (10): :

$$\frac{1}{qt} = \frac{1}{qe} + \frac{1}{k_2 qe qe} \tag{10}$$

where q_e = amount of adsorbed substance (dye) at equilibrium mg/g,

q_t = amount of adsorbed substance (dye) per unit mass at time(mg/g)

K_1 = first order adsorption rate constant (min^{-1}) and t = time (min).

The reaction rate constant k_2 (in g/mg·min) and the equilibrium adsorption capacity are determined from the slope and intercept, respectively, of a linear plot of t/q_t versus t. Kinetic studies of MO dye removal at equilibrium contact time provide valuable insights into the adsorption behavior. The suitability of a kinetic model is assessed by its linear regression value (R^2) being close to 1. Both pseudo-first-order and pseudo-second-order models were applied to the experimental data, as shown in **Figures 13a and 13b,** with the results reported in **Table 4.** When comparing the correlation coefficients, the pseudo-first-order model yielded an R^2 of 0.9136, while the pseudo-second-order model showed a higher R^2 of 0.9676. The higher correlation coefficient for the pseudo-second-order model suggests a better fit to the adsorption data than the pseudo-first-order model. Therefore, the rate control of MO dye removal was primarily governed by chemisorption. This implies that the adsorption mechanism involves valence forces through electron exchange or sharing between

the MO dye molecules and the adsorbent, indicating that the adsorption mechanism is dependent on both the adsorbent and the adsorbate [150, 165, 166].

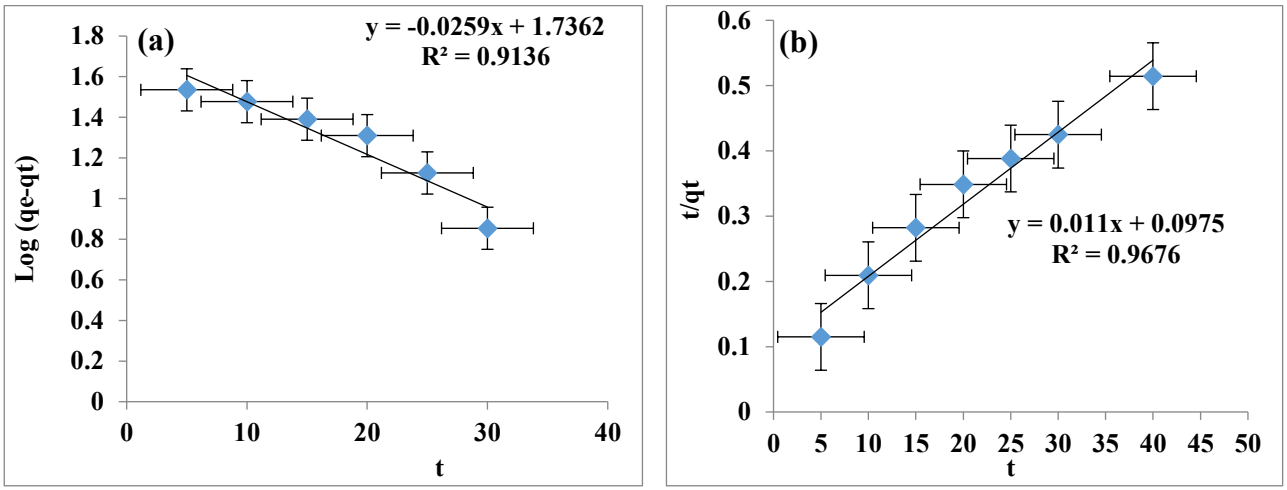

Figure 13. (a) Pseudo–first order and (b) pseudo–second order model

Table 4. Kinetics parameters for pseudo-first order and pseudo–second model

Pseudo-first order	k_1 (min^{-1})	q_e (mg/g)	R^2
	0.05964	54.4753	0.9136
Pseudo-second order	k_2 (g / mg.min)	q_e (mg/g)	R^2
	0.00124	90.9090	0.9676

3.8. Reusability

Figure 14 illustrates the cycling stability of the magnetic adsorbent LB-Fe/Mn. The results show a gradual decrease in the adsorbent's effectiveness with repeated use. While the adsorbent LB-Fe/Mn maintained high removal efficiency for 2-3 cycles, its performance declined to 72.44% by the fifth cycle.

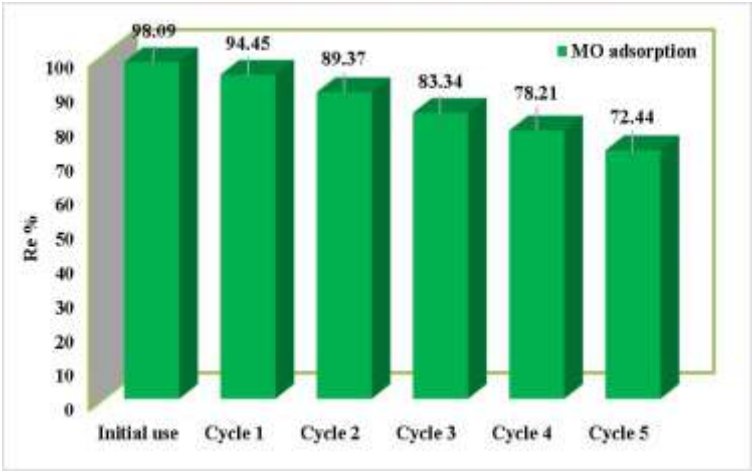

Figure 14. Reuse of LB-Fe/Mn for MO adsorption

3.9. Adsorption mechanism

Lignocellulosic biomass, a generic term referring to the cell walls of plants rich in cellulose, hemicellulose, and lignin, presents an environmental challenge when disposed of. While pure lignocellulose exhibits low adsorption capacity, its effectiveness can be significantly enhanced through modification, leading to cost-effective, lignocellulose-based adsorbent nanocomposites. In this study, a lignocellulose-derived metal/metal oxide nanocomposite was synthesized by doping lignocellulose with manganese and iron via a coprecipitation

method. The Fe/Mn binary oxide was obtained in the form of Fe_3O_4 and MnO_2, as described by the following reaction [65, 167]:

$$3Fe^{+2} + MnO_4^- + 7H_2O = MnO_2 + 3Fe(OH)_3 + 5H^+ \quad (11)$$

The coprecipitation method was also used to synthesize Fe_3O_4-biomass. Here, $Fe(OH)^3$ and $Fe(OH)_2$ were precipitated using $FeCl_3.6H_2O$ and $FeSO_4\,7H_2O$. The lignocellulose's inherent negative charge, primarily due to its hydroxide groups (OH^-), makes it highly effective for removing cationic dyes. Mechanistic studies indicate that the adsorption process involves multiple interactions, including electrostatic forces, hydrogen bonding, $\pi-\pi$ interactions, and pore adsorption. Loading lignocellulose (LB) with $FeCl_3$ and $FeSO_4$ also contributes to an increased surface roughness compared to the raw biomass, further enhancing its adsorption capabilities.

4. Conclusion

This study focused on synthesizing a novel magnetic adsorbent nanocomposite, LB-Fe/Mn, utilizing lignocellulose biomass derived from wood shavings as a raw material. Various techniques were employed for the characterization of the Fe/Mn-modified lignocellulose biomass, all of which confirmed the successful preparation of the adsorbent. The newly developed magnetic adsorbent nanocomposite was then applied to the removal of Methyl Orange (MO) dye from aqueous solutions. The developed LB-Fe/Mn nanocomposite demonstrated excellent removal efficiency (98.16%) for methyl orange, outperforming many current advanced materials. Adsorption data for MO dye best fit the Freundlich isotherm model. Furthermore, thermodynamic studies indicated that the adsorption process is endothermic and spontaneous. Kinetic investigations revealed that adsorption followed a pseudo-second-order model, suggesting a chemical adsorption mechanism. After its useful adsorption life, the spent LB-Fe/Mn adsorbent was collected, dried, and disposed of through controlled landfilling in compliance with local solid waste management guidelines.

Conflict of interest

The authors declare no conflict of interest

References

1. Zolkefli, N., et al., A review of current and emerging approaches for water pollution monitoring. 2020. 12(12): p. 3417.
2. Alprol, A.E., M.S. Gaballah, and M.A.J.R.s.i.m.s. Hassaan, Micro and Nanoplastics analysis: Focus on their classification, sources, and impacts in marine environment. 2021. 42: p. 101625.
3. Abualnaja, K.M., et al., Studying the adsorptive behavior of poly (acrylonitrile-co-styrene) and carbon nanotubes (nanocomposites) impregnated with adsorbent materials towards methyl orange dye. 2021. 11(5): p. 1144.
4. Istratie, R., et al., Single and simultaneous adsorption of methyl orange and phenol onto magnetic iron oxide/carbon nanocomposites. 2019. 12(8): p. 3704-3722.
5. Kadirvelu, K., C. Faur-Brasquet, and P.L.J.L. Cloirec, Removal of Cu (II), Pb (II), and Ni (II) by adsorption onto activated carbon cloths. 2000. 16(22): p. 8404-8409.
6. Mohan, D. and C.U.J.J.o.h.m. Pittman Jr, Activated carbons and low cost adsorbents for remediation of tri-and hexavalent chromium from water. 2006 :(2)137 .p. 762-811.
7. Mohan, D., K.P. Singh, and V.K.J.J.o.h.m. Singh, Trivalent chromium removal from wastewater using low cost activated carbon derived from agricultural waste material and activated carbon fabric cloth. 2006. 135(1-3): p. 280-295.
8. Mohan, D. and K.P.J.W.r. Singh, Single-and multi-component adsorption of cadmium and zinc using activated carbon derived from bagasse—an agricultural waste. 2002. 36(9): p. 2304-2318.
9. Albo Hay Allah, M.A., H.A.J.B.C. Alshamsi, and Biorefinery, Green synthesis of ZnO NPs using Pontederia crassipes leaf extract: characterization, their adsorption behavior and anti-cancer property. 2024. 14(9): p. 10487-10500.
10. Ahmed, T., et al., Climate change, water quality and water-related challenges: a review with focus on Pakistan. 2020. 17(22): p. 8518.

11. Rahman, M.M., et al., Production of functionalized clay-CNC based biopolymeric nanocomposite from agro-waste biomass for bulky industrial wastewater treatment via continuous column adsorption study with mathematical modeling: A critical review. Journal of Cleaner Production, 2025: p. 145883.
12. Rahman, M.M., et al., Fabrication of CNC-AC bionanosorbents from the residual mass of Magnolia champaca l. Bark after methanol extraction for wastewater treatment: Continuous column adsorption study. Environmental Nanotechnology, Monitoring & Management, 2024. 22: p. 101015.
13. Pioli, R.M., et al., Comparison of the effect of N-methyl and N-aryl groups on the hydrolytic stability and electronic properties of betalain dyes. 2020. 183: p. 108609.
14. Mohammed, N., et al., Selective adsorption and separation of organic dyes using functionalized cellulose nanocrystals. 2021. 417: p. 129237.
15. Wang, H., et al., Effective adsorption of dyes on an activated carbon prepared from carboxymethyl cellulose: Experiments, characterization and advanced modelling. 2021. 417: p. 128116.
16. Gupta, V.K.J.J.o.e.m., Application of low-cost adsorbents for dye removal–a review. 2009. 90(8): p. 2313-2342.
17. Wagner, M., et al., Removal of Congo red from aqueous solutions at hardened cement paste surfaces. 2020. 7: p. 567130.
18. Karim, A.N. and L.S. Jasim, Synthesis and characterization of poly (CH/AA-co-AM) composite: Adsorption and thermodynamic studies of benzocaine on from aqueous solutions. International Journal of Drug Delivery Technology, 2019. 9(4): p. 558-562.
19. Zeeshan, M., et al., Investigating the Interactions between Dyes and Porous/Composite Materials: A Comprehensive Study. Sustainable Chemistry for the Environment, 2025 :p. 100217.
20. Abdulhusain, Z.H., L.S. Jasim, and M. Batool, Azur C Dye Removal using GO/P(CMC-Co-Am) Nanocomposite: Adsorption and Kinetic Studies. Journal of Nanostructures, 2024. 14(4): p. 1225-1238.
21. Jamel, H.O., et al., Adsorption of Rhodamine B dye from solution using 3-((1-(4-((1H-benzo[d]imidazol-2-yl)amino)phenyl)ethylidene)amino)phenol (BIAPEHB)/ P(AA-co-AM) composite. Desalination and Water Treatment, 2025. 321.
22. Majeed, H.J., et al., Synthesis and application of novel sodium carboxy methyl cellulose-g-poly acrylic acid carbon dots hydrogel nanocomposite (NaCMC-g-PAAc/ CDs) for adsorptive removal of malachite green dye. Desalination and Water Treatment, 2024. 320.
23. Bafana, A., S.S. Devi, and T.J.E.R. Chakrabarti, Azo dyes: past, present and the future. 2011. 19(NA): p. 350-371.
24. Hosseini, M., et al., Investigations of nickel silicate for degradation of water-soluble organic pollutants. International Journal of Hydrogen Energy, 2024. 61: p. 307-315.
25. Radhy, N.D. and L.S. Jasim ,A novel economical friendly treatment approach: Composite hydrogels. Caspian Journal of Environmental Sciences, 2021. 19(5): p. 841-852.
26. Alyasi, H., H. Mackey, and G.J.M. McKay, Adsorption of methyl orange from water using chitosan bead-like materials :(18)28 .2023 .p. 6561.
27. Bahadi, S.A., et al., Optimization of methyl orange adsorption on MgFeAl-LTH through the manipulation of solution chemistry and synthesis conditions. 2024. 7(3): p. 959-971.
28. Sun, S.-F., et al., Facile construction of lignin-based network composite hydrogel for efficient adsorption of methylene blue from wastewater. 2023. 253: p. 126688.
29. Ai, L., et al., Adsorption of methyl orange from aqueous solution on hydrothermal synthesized Mg–Al layered double hydroxide. 2011. 56 :(11)p. 4217-4225.
30. Ghzal, Q., T. Javed, and M. Batool, Potential of easily prepared low-cost rice husk biochar and burnt clay composite for the removal of methylene blue dye from contaminated water. Environmental Science: Water Research & Technology :(11)9 .2023 ,p. 2925-2941.
31. Kanwal, F., et al., Enhanced dye photodegradation through ZnO and ZnO-based photocatalysts doped with selective transition metals: a review. Environmental Technology Reviews, 2024. 13(1): p. 754-793.
32. Shah, A., et al., The effect of dose, settling time, shelf life, storage temperature and extractant on Moringa oleifera Lam. protein coagulation efficiency. Environmental Nanotechnology, Monitoring & Management, 2024. 21: p. 100919.
33. Shah, A., et al., Adsorptive removal of arsenic from drinking water using KOH-modified sewage sludge-derived biochar. Cleaner Water, 2024. 2: p. 100022.
34. Rengaraj, S., et al., Kinetics of removal of chromium from water and electronic process wastewater by ion exchange resins: 1200H, 1500H and IRN97H. 2003. 102(2-3): p. 257-275.
35. Huang, R., et al., Adsorption of methyl orange onto protonated cross-linked chitosan. 2017. 10(1): p. 24-32.
36. Kant, R.J.J.o.W.R. and Protection, Adsorption of dye eosin from an aqueous solution on two different samples of activated carbon by static batch method. 2012. 4(2): p. 93-98.
37. Rita Kant, R.K., Adsorption of dye Eosin from an aqueous solution on two different samples of activated carbon by static batch method. 2012.
38. Attia, H.G.J.J.o.E. and S. Development, Decolorization of direct blue dye by electrocoagulation process. 2013. 17(1): p. 171-181.
39. Taher, A.M., et al., Applications of Nano Composites for Heavy Metal Removal from Water by Adsorption: Mini Review. Journal of Nanostructures, 2024 :(4)14 .p. 1239-1251.

40. Yagub, M.T., et al., Dye and its removal from aqueous solution by adsorption: a review. 2014. 209: p. 172-184.
41. Barman, P., R. Kadam, and A.J.E.M. Kumar, Lignin-based adsorbent for effective removal of toxic heavy metals from wastewater. 2022. 5(3): p. 923-943.
42. Lalvani, S., A. Hubner, and T.J.E.s. Wiltowski, Chromium adsorption by lignin. 2000. 22(1): p. 45-56.
43. Mohan, D., et al., Single, binary and multi-component adsorption of copper and cadmium from aqueous solutions on Kraft lignin—a biosorbent. 2006. 297(2): p. 489-504.
44. Din, M.I., S. Ashraf, and A.J.S.p. Intisar, Comparative study of different activation treatments for the preparation of activated carbon: a mini-review. 2017. 100(3): p. 299-312.
45. Crist, R.H ,.et al., Heavy metal uptake by lignin: comparison of biotic ligand models with an ion-exchange process. 2002. 36(7): p. 1485-1490.
46. Crist, R.H., et al., Use of a novel formulation of kraft lignin for toxic metal removal from process waters. 2005. 39 :(7)p. 1535-1545.
47. Demirbas, A.J.J.o.h.m., Adsorption of lead and cadmium ions in aqueous solutions onto modified lignin from alkali glycerol delignication. 2004. 109(1-3): p. 221-226.
48. Celik, A. and A.J.E.s. Demirbaş, Removal of heavy metal ions from aqueous solutions via adsorption onto modified lignin from pulping wastes. 2005. 27(12): p. 1167-1177.
49. Fadhil, A.B., M.M.J.A.J.f.S. Deyab, and Engineering, Conversion of some fruit stones and shells into activated carbons. 2008. 33.
50. Shahmohammadi-Kalalagh, S., et al., Isotherm and kinetic studies on adsorption of Pb, Zn and Cu by kaolinite. 2011. 9(2): p. 243-255.
51. Saadallah, K., et al., Potential of the Algerian pine tree bark for the adsorptive removal of methylene blue dye: Kinetics, isotherm and mechanism study. Journal of Dispersion Science and Technology, 2024: p. 1-19.
52. Javed, T., et al., Investigating the adsorption potential of coconut coir as an economical adsorbent for decontamination of lanthanum ion from aqueous solution. Journal of Dispersion Science and Technology, 2024.
53. Arshad, R., T. Javed, and A. Thumma, Exploring the efficiency of sodium alginate beads and Cedrus deodara sawdust for adsorptive removal of crystal violet dye. Journal of Dispersion Science and Technology :(12)45 .2024 , p. 2330-2343.
54. Guo, X., S. Zhang, and X.-q.J.J.o.h.m. Shan, Adsorption of metal ions on lignin. 2008. 151(1): p. 134-142.
55. Guo XueYan, G.X., Z.S. Zhang ShuZhen, and S.X. Shan XiaoQuan, Adsorption of metal ions on lignin. 2008.
56. Ghaffar, S.H., M.J.B. Fan, and bioenergy, Structural analysis for lignin characteristics in biomass straw. 2013. 57: p. 264-279.
57. Kini, M.S., et al., Statistical analysis of Congo Red dye removal using sawdust activated carbon. 2017. 12(19): p. 8788-8804.
58. Hao, Y.S., et al. A review of production, properties and application in scavenging of dyes of biochar. in Third International Conference on Separation Technology 2020 (ICoST 2020). 2020. Atlantis Press.
59. Katika, R.M., et al., Perspectives of Biochar-Aided Advanced Oxidation Processes for the Remediation of Emerging Dyeing Contaminants. 2024.
60. Wu, W., et al., The role of lignin structure on cellulase adsorption and enzymatic hydrolysis. 2023. 3(1): p. 96-107.
61. Sun, Y., et al., Facile synthesis of Fe-modified lignin-based biochar for ultra-fast adsorption of methylene blue: Selective adsorption and mechanism studies. 2022. 344: p. 126186.
62. Collivignarelli, M.C., et al., Preparation and modification of biochar derived from agricultural waste for metal adsorption from urban wastewater. 2024. 16(5): p. 698.
63. Abd Alhussein, M.M. and N.S.J.J.o.N. Salman, Preparation of Nano Lignin–Based Activated Carbon Depending on Ratio Impregnation of K2CO3, Activation Time and Activation Temperature on Yield for Congo Red Dye Adsorption. 2024. 14(3): p. 857-874.
64. da Silva Lacerda, V., et al., Rhodamine B removal with activated carbons obtained from lignocellulosic waste. 2015. 155: p. 67-76.
65. Aziz, S., et al., Green technology: synthesis of iron-modified biochar derived from pine cones to remove azithromycin and ciprofloxacin from water. 2024. 12: p. 1353267.
66. Yu, H., et al., Synthesis of a lignin-Fe/Mn binary oxide blend nanocomposite and its adsorption capacity for methylene blue. 2021. 6 :(26)p. 16837-16846.
67. Javed, T., et al., Sustainable Dye Wastewater Treatment: A Review of Effective Strategies and Future Directions. Physical Chemistry Research, 2025.
68. Urooj, H., et al., Adsorption of crystal violet dye from wastewater on Phyllanthus emblica fruit (PEF) powder: kinetic and thermodynamic. International Journal of Environmental Analytical Chemistry, 2024. 104(19): p. 7474-7499.
69. Bukhari, A., T. Javed, and M.N. Haider, Adsorptive exclusion of crystal violet dye from wastewater by using fish scales as an adsorbent. Journal of Dispersion Science and Technology, 2023. 44(11): p. 2081-2092.
70. Imran, M.S., et al., Sequestration of crystal violet dye from wastewater using low-cost coconut husk as a potential adsorbent. Water Science and Technology, 2022. 85(8): p. 2295-2317.
71. Zainal, N.H., et al., Carbonisation-activation of oil palm kernel shell to produce activated carbon and methylene blue adsorption kinetics. 2018. 30(3): p. 495-502.

72. Geçgel, Ü., et al., Adsorption of cationic dyes on activated carbon obtained from waste Elaeagnus stone. 2016. 34(9-10): p. 512-525.
73. Zghair, A.N., et al., Synthesis, characterization and adsorption properties of azo-functionalized polymeric hydrogels for R6G dye removal from water. Applied Chemical Engineering, 2025. 8.(1)
74. Khan, S.A., et al., Fourier transform infrared spectroscopy: fundamentals and application in functional groups and nanomaterials characterization. 2018: p. 317-344.
75. Zaitan, H. and T.J.C.R.C. Chafik, FTIR determination of adsorption characteristics for volatile organic compounds removal on diatomite mineral compared to commercial silica. 2005. 8(9-10): p. 1701-1708.
76. Batool, M., et al., Exploring the usability of Cedrus deodara sawdust for decontamination of wastewater containing crystal violet dye. 2021. 224: p. 433-448.
77. Hossain, M.I., et al., Preparation and characterization of crystalline nanocellulose from keya (Pandanus tectorius) L. fiber as potential reinforcement in sustainable bionanocomposite: A waste to wealth scheme. Carbohydrate Polymer Technologies and Applications, 2024. 8: p. 100600.
78. Rahman, M.M., et al., Production of cellulose nanocrystals from the waste banana (M. Oranta) tree rachis fiber as a reinforcement to fabricate useful bionanocomposite. Carbohydrate Polymer Technologies and Applications, 2024. 8: p. 100607.
79. Ibarra, D., et al., Chemical characterization of residual lignins from eucalypt paper pulps. 2005. 74(1-2): p. 116-122.
80. Fang, L., et al., Preparation of lignin-based magnetic adsorbent from kraft lignin for adsorbing the Congo red. 2021. 9: p. 691528.
81. Tejado, A., et al., Physico-chemical characterization of lignins from different sources for use in phenol–formaldehyde resin synthesis. 2007. 98(8): p. 1655-1663.
82. Mahdi, M.A., et al., Tailoring the innovative Lu2CrMnO6 double perovskite nanostructure as an efficient electrode materials for electrochemical hydrogen storage application. Journal of Energy Storage, 2024. 88.
83. Kianipour, S., et al., The synthesis of the P/N-type NdCoO3/g-C3N4 nano-heterojunction as a high-performance photocatalyst for the enhanced photocatalytic degradation of pollutants under visible-light irradiation. Arabian Journal of Chemistry, 2022. 15.(6)
84. Al-Nayili, A. and W.A.J.R.o.C.I .Alhaidry, Batch to continuous photocatalytic degradation of phenol using nitrogen-rich g-C3N4 nanocomposites. 2023. 49(10): p. 4239-4255.
85. Zhong, M., Y.-T. Liu, and X.-M.J.J.o.M.C.B. Xie, Self-healable, super tough graphene oxide–poly (acrylic acid) nanocomposite hydrogels facilitated by dual cross-linking effects through dynamic ionic interactions. 2015. 3(19): p. 4001-4008.
86. Dhayal, M., et al., Strategies to prepare TiO2 thin films, doped with transition metal ions, that exhibit specific physicochemical properties to support osteoblast cell adhesion and proliferation. 2014. 37: p. 99-107.
87. Halysh, V., et al., Structural characterization of by-product lignins from organosolv rapeseed straw pulping and their application as biosorbents. 2022. 29(1 :(2p. 510.
88. Mhammed Alzayd, A.A., et al. A new adsorption material based GO/PVP/AAc composite hydrogel characterization, study kinetic and thermodynamic to removal Atenolol drug from wast water. in IOP Conference Series: Materials Science and Engineering. 2020.
89. Razavi, F.S., et al., Fabrication and design of four-component Bi2S3/CuFe2O4/CuO/Cu2O nanocomposite as new active materials for high performance electrochemical hydrogen storage application. Journal of Energy Storage, 2024. 94.
90. AL-Abayechi, M.M.H., A. Al-nayili, and A.A.J.I.C.C. Balakit, Green synthesis of 1, 3-Thiazolidin-4-ones derivatives by using acid-activated montmorillonite as catalyst. 2024. 161: p. 112076.
91. Nirmaladevi, S., N.J.D. Palanisamy, and W. Treatment, A comparative study of the removal of cationic and anionic dyes from aqueous solutions using biochar as an adsorbent. 2020. 175: p. 282-292.
92. Jasim, L.S., et al. Effective adsorptive removal of riboflavin (RF) over activated carbon. in AIP Conference Proceedings. 20 .22AIP Publishing.
93. Mojar Alshamusi, Q.K., et al., Adsorption of crystal violate (CV) dye in aqueous solutions by using P (PVP-co-AAm)/GO composite as (eco-healthy adsorbate surface): characterization and thermodynamics studies. 2021. 21.
94. Kmal, R.Q., et al., Removal of Toxic Congo Red Dye from Aqueous Solution Using a Graphene Oxide/Poly (Acrylamide-Acrylic acid) Hydrogel: Characterization, Kinetics and Thermodynamics Studies. 2022. 12.(4)
95. Ponomarev, N., et al., Lignin-based magnesium hydroxide nanocomposite. Synthesis and application for the removal of potentially toxic metals from aqueous solution. 2019. 2(9): p. 5492-5503.
96. Jalal, N.M., et al. The effect of sulfonation reaction time on polystyrene electrospun membranes as polymer electrolyte. in AIP Conference Proceedings. 2020. AIP Publishing.
97. Adegoke, H., et al., Thermodynamic studies on adsorption of lead (II) Ion from aqueous solution using magnetite, activated carbon and composites. 2017. 21(3): p. 440-452.
98. Osman, A.I., et al., Production and characterisation of activated carbon and carbon nanotubes from potato peel waste and their application in heavy metal removal. 2019. 26: p. 37228-37241.
99. Han, W., et al., Adsorption of bisphenol A on lignin: effects of solution chemistry. 2012. 9: p. 543-548.
100. Zhu, Z., et al., Effect of temperature on methylene blue removal with novel 2D-Magnetism titanium carbide. 2019. 280: p. 120989.

101. Benjedim, S., et al., Synthesis of magnetic adsorbents based carbon highly efficient and stable for use in the removal of Pb (II) and Cd (II) in aqueous solution. 2021. 14(20): p. 6134.
102. AL-Abayechi, M.M.H., A. Al-nayili, and A.A.J.R.o.C.I. Balakit, Montmorillonite clay modified by CuFe2O4 nanoparticles, an efficient heterogeneous catalyst for the solvent-free microwave-assisted synthesis of 1, 3-thiazolidin-4-ones. 2024. 50(4): p. 1541-1556.
103. Widianto, E., et al. Preparation of graphene oxide/poly (3, 4-ethylenedioxytriophene): Poly (styrene sulfonate)(PEDOT: PSS) electrospun nanofibers. in AIP Conference Proceedings. 2016. AIP Publishing.
104. Efelina, V., et al. Preparation of graphene oxide/poly (3, 4-ethylenedioxytriophene): Poly (styrene sulfonate)(PEDOT: PSS) electrospun nanofibers. in AIP Conference Proceedings. 2016. AIP Publishing.
105. Paranthaman, V., et al., Investigation on the performance of reduced graphene oxide as counter electrode in dye sensitized solar cell applications. 2018. 215(18): p. 1800298.
106. Sun, Y., et al., Synthesis of novel lignosulfonate-modified graphene hydrogel for ultrahigh adsorption capacity of Cr (VI) from wastewater. 2021. 295: p. 126406.
107. Lahti, R., et al., Physico-chemical properties and use of waste biomass-derived activated carbons. 2017.
108. Salman, N.S., H.A.J.J.o.P. Alshamsi, and t. Environment, Synthesis of sulfonated polystyrene-based porous activated carbon for organic dyes removal from aqueous solutions. 2022. 30(12): p. 5100-5118.
109. Al-Nayili, A. and S.A.J.J.o.C.S. Haimd, Design of a new ZnCo2O4 nanoparticles/nitrogen-rich g-C3N4 sheet with improved photocatalytic activity under visible light. 2024. 35(1): p. 341-358.
110. Fromm, J., et al., Lignin distribution in wood cell walls determined by TEM and backscattered SEM techniques. 2003. 143(1): p. 77-84.
111. Kayiwa, R ,.et al., Mesoporous activated carbon yielded from pre-leached cassava peels. 2021. 8(1): p. 53.
112. Allah, M.A.A.H., H.K. Ibrahim, and A.A.J.J.o.M.L. Abdulridha, Eco-friendly synthesis of ZnO/chitosan nanocomposite: Detailed characterization, DFT study, docking study, adsorption kinetics, thermodynamic analysis and antioxidant properties. 2025. 425: p. 127216.
113. MUSTAFA, Z., Y. HİKMET, and C. ZEKİ, Thermal, Mechanical and Morphological Properties of Cellulose/Lignin Nanocomposites.
114. Makhado, E. and M.J.J.F.i.c. Hato, Preparation and characterization of sodium alginate-based oxidized multi-walled carbon nanotubes hydrogel nanocomposite and its adsorption behaviour for methylene blue dye. 2021. 9: p. 576913.
115. May, C. and A.J.W.R. Moussa, Chemical and structural analysis of lignocellulosic biomass of Ampelodesmos mauritanicus (DISs) and Stipa tenacissima. 2018. 63: p. 699-712.
116. Zhang, J., et al., Improving lignocellulose thermal stability by chemical modification with boric acid for incorporating into polyamide. 2020. 191: p. 108589.
117. Zhao, W., et al., Monolayer graphene chemiresistive biosensor for rapid bacteria detection in a microchannel. 2020. 2(1): p. 100004.
118. Raghavan, N., S. Thangavel, and G.J.M.S.i.S.P. Venugopal, Enhanced photocatalytic degradation of methylene blue by reduced graphene-oxide/titanium dioxide/zinc oxide ternary nanocomposites. 2015. 30: p. 321-329.
119. Petrie, F.A., et al., Facile fabrication and characterization of kraft lignin@ Fe3O4 nanocomposites using pH driven precipitation: Effects on increasing lignin content. 2021. 181: p. 313-321.
120. Elewa, A.M., et al., Chemically activated carbon based on biomass for adsorption of Fe (III) and Mn (II) ions from aqueous solution. 2023. 16(3): p. 1251.
121. Hambisa, A.A., et al., Adsorption studies of methyl orange dye removal from aqueous solution using Anchote peel-based agricultural waste adsorbent. 2023. 13(1): p. 24.
122. Hu, L., et al., Adsorption behavior of dyes from an aqueous solution onto composite magnetic lignin adsorbent. 2020. 246: p. 125757.
123. Abbas, M., M.J.P.s. Trari, and E. protection, Kinetic, equilibrium and thermodynamic study on the removal of Congo Red from aqueous solutions by adsorption onto apricot stone. 2015. 98: p. 424-436.
124. Hanum, L., et al., The adsorption capacity of methylene blue by activated carbon immobilized yarn. 2022. 15(03): p. 1965-1974.
125. Abdu, M., et al., The development of Giant reed biochar for adsorption of Basic Blue 41 and Eriochrome Black T. azo dyes from wastewater. 2024. 14(1): p. 18320.
126. Yang, J., et al. Study on adsorption of chromium (VI) by activated carbon from cassava sludge. in IOP conference series: earth and environmental science. 2018. IOP Publishing.
127. Banerjee, S. and M.J.A.J.o.C. Chattopadhyaya, Adsorption characteristics for the removal of a toxic dye, tartrazine from aqueous solutions by a low cost agricultural by-product. 2017. 10: p. S1629-S1638.
128. Wang, P., T. Yan, and L.J.B. Wang, Removal of Congo red from aqueous solution using magnetic chitosan composite microparticles. 2013. 8(4): p. 6026-6043.
129. Wang Peng, W.P., Y.T. Yan TingGuo, and W.L. Wang LiJuan, Removal of Congo red from aqueous solution using magnetic chitosan composite microparticles. 2013.
130. Alam, M.S., R .Khanom, and M.A.J.A.J.o.E.P. Rahman, Removal of Congo red dye from industrial wastewater by untreated sawdust. 2015. 4(5): p. 207.
131. Abbas, A., et al., Isothermal Evaluation of Chemical Modification of Ricinus communis Stem Used for Adsorptive Removal of Brilliant Blue FCF Dye from Water. 2013. 25.(16)

132. Aadil Abbas, A.A., et al., Isothermal evaluation of chemical modification of Ricinus communis stem used for adsorptive removal of Brilliant blue FCF dye from water. 2013.
133. Vimonses, V., et al ,.Adsorption of congo red by three Australian kaolins. 2009. 43(3-4): p. 465-472.
134. Bedmohata, M., et al., Adsorption capacity of activated carbon prepared by chemical activation of lignin for the removal of methylene blue dye. 2015. 2(8): p. 1-13.
135. Liu, Z. and Y.J.J.o.C. Wei, K2CO3 ‐ Activated Pomelo Peels as a High ‐ Performance Adsorbent for Removal of Cu (II): Preparation, Characterization, and Adsorption Studies. 2021. 2021(1): p. 9940577.
136. Murcia-Salvador, A., et al., Adsorption of Direct Blue 78 using chitosan and cyclodextrins as adsorbents. 2019. 11(6): p. 1003.
137. Rezaei, H., A. Razavi, and A.J.E.R.R. Shahbazi, Removal of Congo red from aqueous solutions using nano-chitosan. 2017. 5(1): p. 25-34.
138. N. Zghair, A., et al., Synthesis, characterization and adsorption properties of azo-functionalized polymeric hydrogels for R6G dye removal from water. Applied Chemical Engineering, 2025. 8(1): p. ACE-5604.
139. Javed, T., et al., Batch adsorption study of Congo Red dye using unmodified Azadirachta indica leaves: isotherms and kinetics. Water Practice & Technology, 2024. 19(2): p. 546-566.
140. Salmam, N.S., H.K. Dakheel, and A.J.J.E.J.o.C. Kadhim, Study of thrmodynamic values in different temperature from partition coefficient for some organic acids immiscible di-solvents mixtures. 2021. 64(12): p. 7417-7420.
141. Kılıç, M., A.S.K.J.B.I.J.o.S. Janabi, and T. Research, Investigation of dyes adsorption with activated carbon obtained from Cordia myxa. 2017. 1(2): p. 87-104.
142. Jedynak, K., et al., Mesoporous carbons as adsorbents to removal of methyl orange (anionic dye) and methylene blue (cationic dye) from aqueous solutions. 2021. 220: p. 363-379.
143. Shayesteh, H., et al., Trimethylamine functionalized clay for highly efficient removal of diclofenac from contaminated water: experiments and theoretical calculations. 2020. 20: p. 100615.
144. Sun, Y., et al., Removal of Pollutantswith Activated Carbon Produced from K2CO3 Activation of Lignin From Reed Black Liquors. 2006. 20(4): p. 429-43.5
145. Shah, A., et al., Sequential novel use of Moringa oleifera Lam., biochar, and sand to remove turbidity, E. coli, and heavy metals from drinking water. Cleaner Water, 2024. 2: p. 100050.
146. Joshi, S. and B.P.J.J.o.t.I.o.E. Pokharel, Preparation and characterization of activated carbon from lapsi (Choerospondias axillaris) seed stone by chemical activation with potassium hydroxide. 2013. 9(1): p. 79-88.
147. Tekin, B. and U.J.G.U.J.o.S. Açıkel, Adsorption isotherms for removal of heavy metal ions (copper and nickel) from aqueous solutions in single and binary adsorption processes. 2022. 36(2): p. 495-509.
148. Nunes, N., M.T. Santos, and A.J.J.o.t.B.C.S. Martins, Low cost modified biochars from peanut shells for the removal of textile dyes. 2023 :(6)34 .p. 885-893.
149. Ghane, S., et al., Insights into the impacts of synthesis parameters on lignin-based activated carbon and its application for: methylene blue adsorption. 2023. 57(1): p. 111-132.
150. Wanyonyi, W.C., J.M. Onyari, and P.M.J.E.P. Shiundu, Adsorption of Congo red dye from aqueous solutions using roots of Eichhornia crassipes: kinetic and equilibrium studies. 2014. 50: p. 862-869.
151. Abazli, H., H. Jneidi, and S.J.B.S.J. Hatem, Kinetic, isotherm and thermodynamic studies on the ciprofloxacin adsorption from aqueous solution using aleppo bentonite. 2022. 19(3): p. 0680-0680.
152. Pascu, D.-E., et al., Iron and manganese removal from drinking water. 2016. 6(1): p. 47-55.
153. Eskandarian, L., et al., Evaluation of adsorption characteristics of multiwalled carbon nanotubes modified by a poly (propylene imine) dendrimer in single and multiple dye solutions: isotherms, kinetics, and thermodynamics. 2014. 59(2): p. 444-454.
154. Nechifor, G., et al., Comparative study of Temkin and Flory-huggins isotherms for adsorption of phosphate anion on membranes. 2015. 77(2): p. 63-72.
155. Dada, A., et al., Langmuir, Freundlich, Temkin and Dubinin–Radushkevich isotherms studies of equilibrium sorption of Zn2+ unto phosphoric acid modified rice husk :(1)3 .2012 .p. 38-45.
156. Ao, D., L. AP, and O.J.I.J.o.A.C. AM, Langmuir, Freundlich, Temkin and Dubinin–Radushkevich isotherms studies of equilibrium sorption of Zn 2+ unto phosphoric acid modified rice husk. 2012. 3(1): p. 38-45.
157. Azhar-ul-Haq, M ,.et al., Adsorptive removal of hazardous crystal violet dye onto banana peel powder: equilibrium, kinetic and thermodynamic studies. Journal of Dispersion Science and Technology, 2022: p. 1-16.
158. Priyadarshini, B., et al. Kinetics, Thermodynamics and Isotherm studies on Adsorption of Eriochrome Black-T from aqueous solution using Rutile TiO2. in IOP Conference Series: Materials Science and Engineering. 2018. IOP Publishing.
159. Khan, A., et al., Improvement of the adsorption efficiency of rice husk ash for crystal violet dye removal from aqueous medium. 2022. 65(131): p. 427-435.
160. Cotoruelo, L.M., et al., Adsorbent ability of lignin-based activated carbons for the removal of p-nitrophenol from aqueous solutions. 2012. 184: p. 176-183.
161. Massoud ,M., et al., Removal of Cadmium (II) from aqueous solutions onto Dodonaeae Viscose Leg powder using a green process: Isotherms, Kinetics and Thermodynamics. 2019. 10(1): p. 10-16.
162. Barakan, S., et al., Thermodynamic, kinetic and equilibrium isotherm studies of As (V) adsorption by Fe (III)-impregnated bentonite. 2020. 22: p. 5273-5295.

163. Sharma, R., et al., Kinetics and adsorption studies of mercury and lead by ceria nanoparticles entrapped in tamarind powder. 2018. 3(11): p. 14606-14619.
164. Tan ,K. and B.J.J.o.t.T.I.o.C.E. Hameed, Insight into the adsorption kinetics models for the removal of contaminants from aqueous solutions. 2017. 74: p. 25-48.
165. Liu, Y., et al., Simultaneous removal of methyl orange and Cr (VI) using polyethyleneimine-modified corncob-derived carbon material. 2020. 15(4): p. 7342.
166. Rouf, S., M. Nagapadma, and R.R.J.I.J.E.R.A. Rao, Removal of harmful textile dye congo red from aqueous solution using chitosan and chitosan beads modified with CTAB. 2015. 5(3): p. 75-82.
167. Do, P.M.T., et al., Removal of Anions PO 4 3-and Methyl Orange Using Fe-Modified Biochar Derived from Rice Straw. 2023. 42.(3)